PHYSICS

Atom interferometry with thousand-fold increase in dynamic range

Dimitry Yankelev[1,2*†], Chen Avinadav[1,2†], Nir Davidson[1], Ofer Firstenberg[1]

The periodicity inherent to any interferometric signal entails a fundamental trade-off between sensitivity and dynamic range of interferometry-based sensors. Here, we develop a methodology for substantially extending the dynamic range of such sensors without compromising their sensitivity, stability, and bandwidth. The scheme is based on simultaneous operation of two nearly identical interferometers, providing a moiré-like period much larger than 2π and benefiting from close-to-maximal sensitivity and from suppression of common-mode noise. The methodology is highly suited to atom interferometers, which offer record sensitivities in measuring gravito-inertial forces but suffer from limited dynamic range. We experimentally demonstrate an atom interferometer with a dynamic-range enhancement of more than an order of magnitude in a single shot and more than three orders of magnitude within a few shots for both static and dynamic signals. This approach can considerably improve the operation of interferometric sensors in challenging, uncertain, or rapidly varying conditions.

INTRODUCTION

The ambiguity-free dynamic range of interferometric physical sensors is fundamentally limited to 2π radians. When the a priori phase uncertainty is larger than a single fringe, additional information is required to uniquely determine the physical quantity measured by the interferometer. If this quantity remains constant over long periods of time, then the phase ambiguity may be resolved through additional interferometric measurements with different scale factors, defined as the ratio between the interferometer phase and the magnitude of the physical quantity. A more challenging scenario arises when the physical quantity changes rapidly with time, and measurement with multiple scale factors must be realized simultaneously.

Overcoming this challenge in cold-atom interferometers (*1*), which have emerged over the past decades as extremely sensitive sensors of gravitational and inertial forces, is an especially ambitious proposition. Applications of atom interferometers vary from fundamental research (*2*–*6*) and precision measurements (*7*, *8*) to gravity surveys and inertial navigation (*9*). Mobile interferometers are being developed by several groups (*10*–*13*) with demonstrations of land-based, marine, and airborne gravity surveys (*14*–*16*).

In the latter applications, limited dynamic range is especially challenging, as the uncertainty in the acceleration to be measured is potentially very large. Reducing the interferometer scale factor or performing multiple measurements at each location results in reduced sensitivity or lower temporal bandwidth, respectively. A possible solution relies on auxiliary acceleration sensors with larger dynamic range but lower stability to constrain the interferometric measurement to a smaller, nonambiguous range (*17*, *18*). This hybrid approach has been previously used for mobile inertial measurements, e.g., on ships (*14*) and airplanes (*16*, *19*). However, it requires that the uncertainty in acceleration estimation from the auxiliary sensor be smaller than the 2π periodicity of the interferometric sensor. This may be difficult to achieve when operating the interferometer at maximum sensitivity owing to large variations in the auxiliary sensor bias, transfer function errors, misalignment between the sensors, or nonlinearities. Increasing the interferometer dynamic range beyond 2π would reduce sensitivity to such effects and enable hybrid operation under more challenging conditions. It is therefore highly desirable to have a high-sensitivity, high-bandwidth atom interferometer with a large dynamic range. While optical interferometers may gain such capabilities by using and detecting multiple wavelengths (*20*, *21*), this feat is more challenging for matter-wave interferometers.

In this work, we achieve a substantial enhancement of dynamic range on a single-shot basis by combining two powerful approaches in atom interferometry: increasing the dynamic range without sensitivity loss through small variations of the interferometer scale factor (*22*) and acquiring multiple phase measurements in a single experimental run (*23*, *24*). First, when the same fundamental physical quantity determines two interferometric phases with slightly different scale factors, it can be uniquely extracted within an enhanced dynamic range, determined by a moiré wavelength, which is inversely proportional to the difference between scale factors (Fig. 1A). Second, by operating and reading out the two interferometers simultaneously within the same experimental shot, major common-mode noises are efficiently rejected, increasing the scheme's robustness to dominant sources of noise. In addition, such operation maintains the original temporal bandwidth of the measurement. Further exponential increase in dynamic range, at the cost of a linear reduction of temporal bandwidth, is achieved by varying the scale factor ratio between shots.

RESULTS

Principles of dual-*T* interferometry

We realize the above concept in a Mach-Zehnder atom interferometer measuring the local acceleration of gravity (*25*). Such devices use light pulses as "atom optics" that split the atomic wave packet into two arms and later recombine them after they traveled on macroscopically distinct trajectories. The differential phase accumulated between the arms of the interferometer depends on the motion of the atoms.

In our experiment, laser-cooled ^{87}Rb atoms are launched vertically on a free-fall trajectory. Counterpropagating, vertical laser beams at 780 nm drive two-photon Raman transitions between two

[1]Department of Physics of Complex Systems, Weizmann Institute of Science, Rehovot 7610001, Israel. [2]Rafael Ltd., Haifa 3102102, Israel.
*Corresponding author. Email: dimitry.yankelev@weizmann.ac.il
†These authors contributed equally to this work.

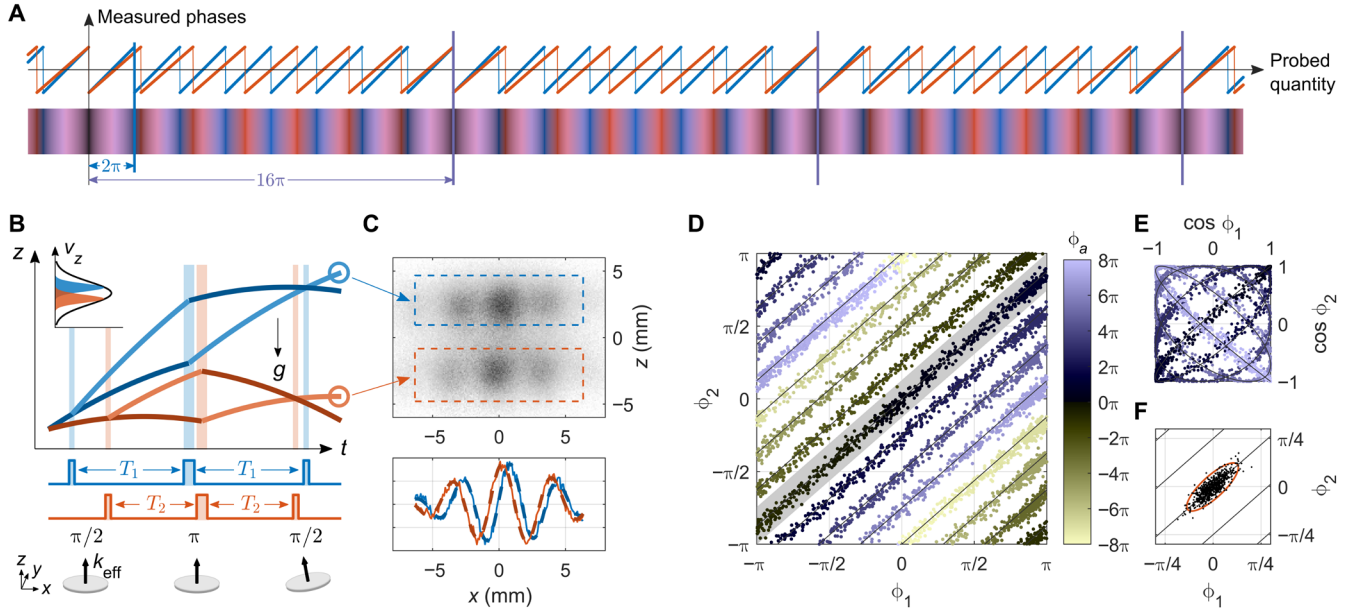

Fig. 1. Concept, scheme, and results of dual-*T* interferometry. (**A**) Conceptual representation of dynamic range enhancement by a factor of ×8, using a pair of simultaneous interferometers with different scale factors. (**B**) Dual-*T* atom interferometry. A pair of Raman pulse sequences (red and blue), with different interrogation times *T* and addressing different velocity classes of the atoms, coupled between two atomic states with a momentum difference of $\hbar k_{\mathrm{eff}}$ (bright and dark trajectories). To obtain full phase quadrature information, the Raman retro-reflecting mirror is tilted before the final π/2 pulses, generating a transverse phase gradient across the cloud. (**C**) Top: A single fluorescence image captures the population in one of the atomic states for both interferometers. Bottom: Measured cross sections (solid lines) and the fitted fringes (dashed lines) of both interferometers, after vertical integration of the regions indicated by the dashed rectangles and subtraction of the Gaussian envelope. The interferometer phases ϕ_1, ϕ_2 are determined by the fringe phase at the center of each cloud. (**D**) Results of dual-*T* interferometry for inertial phase ϕ_a in the range of ±8π (color-coded); each dot represents a single dual-*T* measurement. Slope of gray lines is the scale factor ratio $\tau = (T_2/T_1)^2 = 7/8$. Shaded region represents the original, ambiguity-free, 2π dynamic range of a single interferometer operated at $T = T_1$. Full-quadrature phase detection allows for a unique solution for all phases, compared to ambiguities generated when detecting only the cosine component (**E**). (**F**) Dual-*T* measurements at constant inertial phase $\phi_a = 0$, demonstrating that the noise in both interferometers is highly correlated with slope ∼τ. In red, the covariance ellipse at 95% confidence level.

electronic ground states while imparting recoil of two photon momenta (*26*). The Raman beams are sent from the top and are retro-reflected from a mechanically stabilized mirror at the bottom, which defines the reference frame with respect to which the motion of the atoms is measured. The interferometric sequence is composed of three Raman pulses, equally spaced by time *T*, acting to split the atomic wave packet into two components that drift apart, and then to redirect and recombine them, leading to a final atomic population ratio determined by the phase difference between the two arms.

In this configuration, the phase difference is determined by the gravitational acceleration *g* according to $\phi_a = (k_{\mathrm{eff}}g - \alpha)T^2$, with $\hbar k_{\mathrm{eff}}$ as the total momentum transferred by the Raman interaction and α as a chirp rate applied to the relative frequency between the Raman beams to compensate for the changing Doppler shift of the falling atoms. Residual vibrations of the mirror contribute noise to the inertial phase ϕ_a.

The concept we develop relies on a so-called dual-*T* operation of the interferometer. Instead of one pulse sequence, two interleaved pulse sequences with slightly different *T* values are performed (Fig. 1B). Raman transitions with counterpropagating beams are Doppler sensitive; that is, they efficiently address atoms only within a narrow distribution of vertical velocities. Therefore, by tuning the two-photon Doppler detuning of each set of pulses, one can independently address different velocity classes of the atoms (inset in Fig. 1B). We operate the two interferometers with scale factors differing by the ratio $\tau \lesssim 1$, choosing the interferometric durations $T_1 = T$ and $T_2 = \sqrt{\tau}\,T$, with $T = 55$ ms (see Materials and Methods).

Conventionally, the population ratio between the interfering atomic states is measured directly, and the cosine of the phase is extracted. In contrast, in our dual-*T* scheme, we detect the phases ϕ_1, ϕ_2 of both interferometers by acquiring an image of the atoms in one of the final atomic states. We obtain the phase through phase shear readout (*27*), tilting the retro-reflecting Raman mirror by a small angle before the final π/2 pulses to add a horizontal phase gradient, and thereby generate a spatial transverse interference pattern across the cloud, as used in point-source interferometry (*28*–*30*). This detection method offers two advantages. First, the phase offset of the spatial interference pattern is directly extracted with constant sensitivity for all interferometric phases, in a manner equivalent to full quadrature detection, where both sine and cosine components of the phase are measured. Second, independent readout of both interferometers is inherently achieved owing to the mapping of the different velocity classes onto different vertical positions, due to ballistic expansion of the cloud. A typical image obtained in a single experiment is shown in Fig. 1C.

Figure 1D shows single-shot measurements in a dual-*T* operation with the dynamic range enhanced by a factor of 8. We vary ϕ_a by changing the chirp rate α with respect to its nominal value $\alpha_0 = k_{\mathrm{eff}}g$, thereby emulating changes in *g*. According to the equivalence principle, the scenario of the mirror being at rest with the lasers chirped at $k_{\mathrm{eff}}(g - a)$ and the scenario of the mirror accelerating at $a \neq 0$ while the lasers are chirped at $k_{\mathrm{eff}}g$ are indistinguishable from the point of view of the atoms. Varying the chirp rate is therefore the standard method to emulate changes in acceleration in a precise

and controlled manner. We find that ϕ_a is mapped onto a unique set of straight, parallel lines in the plane spanned by ϕ_1 and ϕ_2 owing to the quadrature detection capability. Conversely, conventional detection, which resolves only the cosine of the phase, would result in many phase ambiguities due to very different values of ϕ_a being mapped to similar measured phase components (Fig. 1E), severely limiting the benefits of a dual-T operation. Quadrature detection, together with the strong suppression of common noise due to operation at very similar scale factors, allows the dual-T scheme to achieve a considerably larger enhancement compared to past implementations of simultaneous atom interferometers with different scale factors (*23*).

Phase estimation for single-shot dual-*T*

The measured interferometric phases ϕ_1, ϕ_2 are constrained to the bare dynamic range $\pm\pi$ and can be written as

$$\phi_1 = \phi_a - 2\pi n_1 \quad (1)$$

$$\phi_2 = \tau\phi_a - 2\pi n_2 \quad (2)$$

The integers n_1 and n_2, which respectively bring ϕ_1 and ϕ_2 to the range $\pm\pi$, are a priori unknown.

We define $D \equiv (1-\tau)^{-1}$, with $\tau = (T_2/T_1)^2$ as the scale factor ratio. For integer values of D, the dynamic range enhancement is exactly D; as illustrated in Fig. 1A, ϕ_1 and ϕ_2 have a joint period of $2D\pi$ as in a moiré effect, resulting in an extended ambiguity-free dynamic range of $\pm D\pi$ (see Materials and Methods for discussion on noninteger values).

To analyze a dual-T measurement and extract an estimate for ϕ_a, we define the quantities ϕ_{diff} and ϕ_{sum}

$$\begin{pmatrix}\phi_{\mathrm{diff}}\\ \phi_{\mathrm{sum}}\end{pmatrix} = \frac{1}{1+\tau^2}\begin{pmatrix}\tau & -1\\ 1 & \tau\end{pmatrix}\begin{pmatrix}\phi_1\\ \phi_2\end{pmatrix} \quad (3)$$

ϕ_{diff} and ϕ_{sum} act as coarse and fine measurements, respectively. As shown in Fig. 2A, which presents an analysis of $D = 8$ dual-T measurements, ϕ_{diff} takes on a discrete set of $2D - 1$ values. This constrain uniquely determines the values of n_1 and n_2 and hence the 2π subrange in which ϕ_a lies. Correspondingly, ϕ_{sum} is a continuous variable, providing the estimation of the inertial phase ϕ_a within that subrange (see Materials and Methods).

Phase estimation for sequential operation

We now turn to discuss further enhancement of the dynamic range obtained by a sequence of several dual-T shots with alternating integer values of D. Here, we fix T_1 and alternate T_2 between shots. Assuming that changes in ϕ_a are smaller than π between consecutive shots, the above analysis per shot provides n_1 mod D. Together, the full sequence uniquely determines n_1 within a range defined by the least common multiple of the used D values, or, for coprime integers, simply their product (see Materials and Methods and fig. S1).

Analyses of two-shot operation with $D = 7,8$ and three-shot operation with $D = 5,7,8$ are shown in Fig. 2 (B and C). Each data point is a measurement with a random value of ϕ_a within the extended dynamic ranges $\pm 56\pi$ and $\pm 280\pi$, respectively. We observe two- and three-dimensional clustering of the differential phases ϕ_{diff}, where each cluster corresponds to a unique, nonambiguous phase range smaller than 2π.

Noise and outlier probability

By virtue of simultaneously operating the two interferometers with similar scale factors, vibration-induced phase noise is highly correlated between them (Fig. 1F) and has negligible contribution to ϕ_{diff}. The dominant noise in ϕ_{diff} results from uncorrelated, independent detection noise in ϕ_1 and ϕ_2, whose SD we denote as σ_{ind} (see Materials and Methods for a detailed discussion of noise terms).

As D is increased and the discrete values of ϕ_{diff} become denser, the uncorrelated noise may lead to errors in determining the correct subrange for ϕ_a, producing an outlier with phase estimation error in multiples of 2π. The probability ϵ for a measurement to be such an outlier is approximately (see Eq. 10 for exact expression)

$$\epsilon \approx \mathrm{erfc}\left(\frac{\pi}{2}\frac{1}{D\cdot\sigma_{\mathrm{ind}}}\right) \quad (4)$$

Crucially, ϵ depends only on the uncorrelated noise and not on the vibration-dominated correlated noise, which is typically much larger. In the data presented in Fig. 2A, we observe one such outlier out of 5000 measurements for $D = 8$.

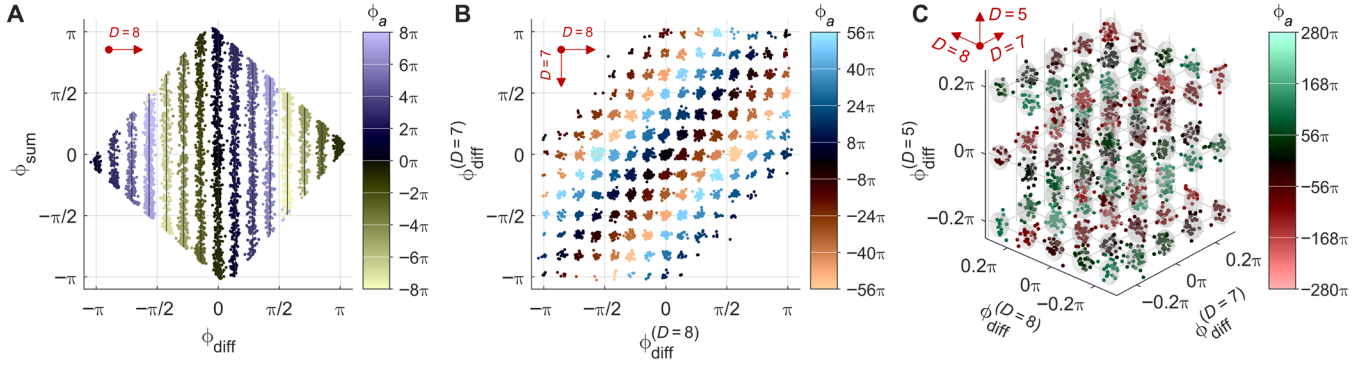

Fig. 2. Analysis of dual-*T* interferometry measurements in single-shot, two-shot, and three-shot operation. (**A**) Single-shot dual-T operation with $D = 8$ for ϕ_a in the range of $\pm 8\pi$ (color-coded). Every dot corresponds to a single measurement. Each discrete value of ϕ_{diff} corresponds to a different subrange of ϕ_a, and within that subrange, ϕ_{sum} changes continuously and linearly with ϕ_a. (**B**) Sequential two-shot dual-T operation with $D = 7,8$ for ϕ_a in the range of $\pm 56\pi$, presented in the $\phi_{\mathrm{diff}}^{(D=7)} - \phi_{\mathrm{diff}}^{(D=8)}$ plane. The discrete clusters in this plane correspond to different subranges of ϕ_a. (**C**) Sequential three-shot dual-T operation with $D = 5,7,8$ for ϕ_a in the range of $\pm 280\pi$, presented in the $\phi_{\mathrm{diff}}^{(D=5)} - \phi_{\mathrm{diff}}^{(D=7)} - \phi_{\mathrm{diff}}^{(D=8)}$ space. For clarity, only a subset of the solutions around $\phi_{\mathrm{diff}}^{(D=5,7,8)} = 0$ is presented, and gray ovals surround the expected solutions.

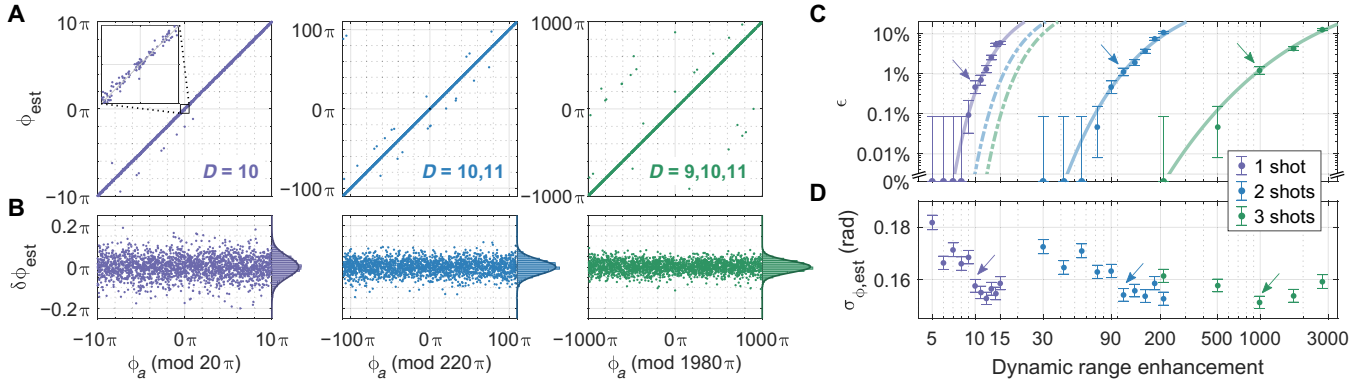

Fig. 3. Performance analysis of dual-*T* interferometry. (**A**) Estimated inertial phase for single-shot measurements (left, inset shown zoom on ±π/2 region) and for sequential two-shot (center) and three-shot (right) measurements, with dynamic range enhancement factors of 10, 110, and 990, respectively. Outlying measurements appear as data points visibly distant (>2π) from their expected value. We observe only 10, 24, and 26 such outliers of 2000 data points in the three datasets, respectively. (**B**) Residuals of the estimated phases, including only non-outlying measurements. Compared to single-shot measurements, SDs of two- and three-shot residuals are smaller by factors of $\sqrt{2}$ and $\sqrt{3}$, respectively. (**C**) Outlier probability ϵ as a function of dynamic range enhancement obtained for individual values of *D* and for various combinations of consecutive coprime *D* values. For $D \leq 8$, there were no outliers in the measured dataset. Error bars represent 67% confidence intervals of the estimated value. Solid lines are calculated using Eq. 4 with $\sigma_{ind} = 80$ mrad. Dashed lines represent outlier probability for an alternative scheme of averaging two or three sequential shots using a single *D* value. (**D**) Estimation error of gravitation phase per shot $\sigma_{\phi,est}$. The error is dominated by vibration-induced phase noise and is nearly equal for all realizations. Arrows in (C) and (D) indicate the measurements shown in (A) and (B).

For the case of sequential dual-*T* operation, the total outlier probability depends on the outlier probabilities in each shot and, in the relevant regime of small error probabilities, is given simply by their sum. For any desired dynamic range and temporal bandwidth, the outlier probability is therefore minimized by choosing consecutive coprime values of *D*.

Experimental performance

To quantify the performance of the dual-*T* scheme in terms of phase sensitivity and outlier probability, we extend the phase scan to random, known, values of ϕ_a within the range of ±1000π, corresponding to accelerations of ±65 mm/s^2 at $T = 55$ ms. For each phase, we perform measurements with *D* values between 5 and 15 and perform dual-*T* analysis using each *D* separately, using pairs of consecutive *D* values, and using triplets of consecutive coprime *D* values. We analyze each measurement within its appropriate extended dynamic range; data points that are outside the measurement's relevant dynamic range are wrapped back onto it. We then compare the extracted phase to its expected value, from which we estimate the outlier probability ϵ as well as the phase residuals of the measurements without outliers.

The results, presented in Fig. 3, demonstrate an enhancement of dynamic range by factors of 10 in a single shot, ~100 in two shots, and ~1000 in three shots, while maintaining phase residuals of $\sigma_{\phi,est}$ ~160 per shot (~3.3 μm/s^2 per shot), and with outlier probabilities of 0.5, 1.1, and 1.2%, respectively. In general, we find excellent agreement with the error model described in Eq. 4, with σ_{ind} = 80 mrad estimated from these data (see the Supplementary Materials).

We note that an outlier fraction on the order of 1% is acceptable in most applications, as such outliers can be identified and removed by comparison to adjacent shots or using auxiliary measurements. However, even if nearly zero outlier fraction is required, the dual-*T* scheme can deliver a substantial dynamic range enhancement. For example, with the above measured value of σ_{ind} and for $D = 6$, we expect $\epsilon \approx 3 \times 10^{-6}$.

Furthermore, averaging over *N* repeated measurements with the same *D* value can decrease the outlier probability ϵ by effectively reducing σ_{ind} by a factor $\sqrt{N}$. However, by using the same number of sequential measurements with alternating values of *D* as described above, the same value of ϵ may be achieved with considerably larger dynamic range enhancement, as seen from comparing solid and dashed curves in Fig. 3C.

Stability of dual-*T* interferometry

To demonstrate the long-term stability of dual-*T* interferometry, we continuously measure gravity over 20 hours with $D = 10$. As shown in Fig. 4, ϕ_a follows the expected tidal gravity variations throughout the measurement period. It remains stable at time scales of 10^4 s to better than 100 nm/s^2, consistent with past gravimetric measurements in our apparatus, showing that the dual-*T* scheme does not add visible drifts to the estimated phase. Therefore, it is possible to reach the same accuracy as conventional interferometric operation relying on a one-off calibration run. Conversely, ϕ_{diff} does exhibit small drifts, which we attribute to mutual light shift between the two interferometers. However, due to the discrete nature of ϕ_{diff}, these drifts can be easily corrected in several ways (see Materials and Methods).

Tracking fast-varying signals

We now turn to discuss dynamic scenarios, such as mobile gravity surveys or inertial measurements on a navigating platform, where the measured acceleration and thus ϕ_a change substantially between shots. Dual-*T* interferometry with fixed *D* can directly track a signal that randomly varies by up to ±*D*π from shot to shot. Moreover, alternating the value of *D* between consecutive measurements can enable tracking a signal with even larger variations; however, the sequential analysis described above cannot be applied due to the phase changing between shots, and a different analysis method is required.

To track such a signal, we use a particle filter estimation protocol (*31*, *32*). Particle filtering is a powerful and well-established technique in navigation science, signal processing, and machine learning, among other fields. It is a sequential, Monte Carlo estimation approach based on a large number of particles, which represent possible hypotheses of the system's current state, e.g., the inertial

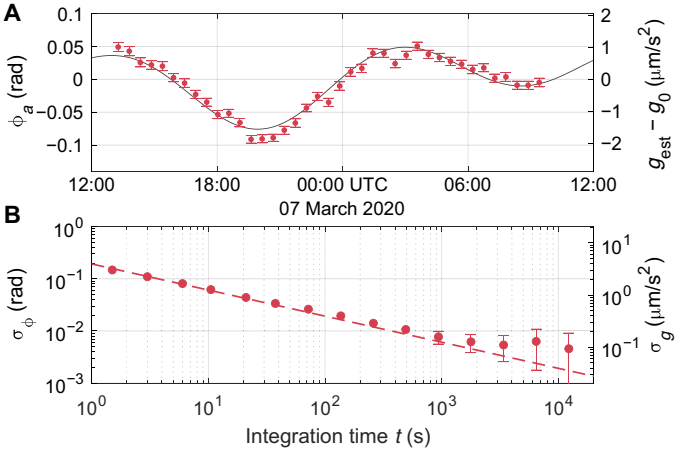

Fig. 4. Stability of dual-*T* interferometry. (**A**) Time series of ϕ_{sum}, with half-hour binning, measured with $D = 10$. The results follow the expected tidal gravity variation as calculated from solid-earth model (black solid line). UTC, universal time coordinated. (**B**) Allan deviation of the residuals of ϕ_{sum} from the tidal model. The dashed line is a fit to $t^{-1/2}$ with a sensitivity per shot of 155 mrad (3.2 μm/s^2).

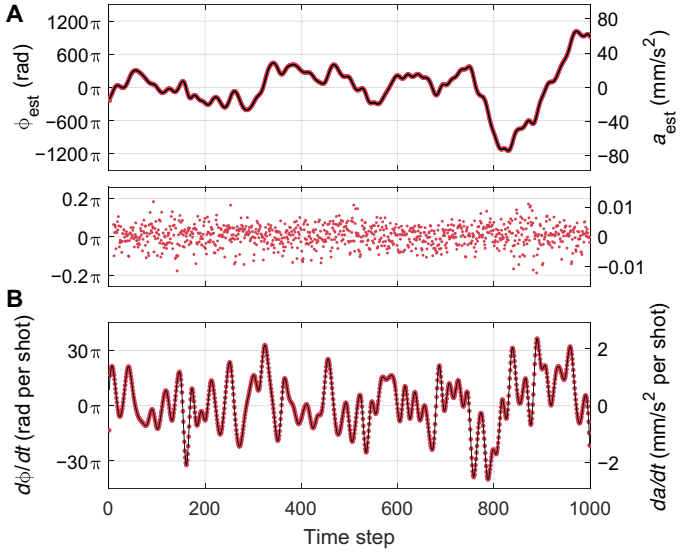

Fig. 5. Tracking of a time-varying acceleration using dual-interferometry combined with a particle filter protocol. Measurements are performed with alternating $D = 9,10$. (**A**) Acceleration signal extracted from the measurements using the particle filter (red), compared to the input signal (black). Bottom panel shows the residuals with an SD of 174 mrad (3.6 μm/s^2). (**B**) Temporal derivative (shot-to-shot variation) of the measured acceleration signal (red) compared to the input (black).

phase measured by the sensor. These hypotheses are weighted through Bayesian estimation after every measurement, converging on a solution that is consistent with the sensor readings over time. In our context, under some model assumptions on the signal dynamics, use of particle filter enables full recovery of the single-shot bandwidth (*22*) while maintaining the large increase in dynamic range rendered by the sequential operation.

An experimental realization of tracking a dynamic signal is presented in Fig. 5. We change the chirp rate α between shots to simulate a band-limited random walk of a and perform dual-T measurements with alternating $D = 9,10$. The sequence of measured phases is then analyzed with a particle filter protocol using a second-order derivative model (see Materials and Methods) to extract best estimate for the time series of ϕ_a. Following a brief convergence period (fig. S6), we successfully track this time-varying signal, which spans over 2000π and changes by up to 40π between shots, with sensitivity per shot similar to measurements of static signals under similar conditions and with no outliers. We note that while the analysis was carried out in post-process, it is in principle compatible with implementation as a real-time protocol.

DISCUSSION

In conclusion, we present an approach to atom interferometry for substantial enhancement of dynamic range without compromising sensitivity and measurement bandwidth. In applications where traditional atom interferometers must be operated at reduced sensitivity owing to the expected dynamic range of the measured signal, our approach enables measurements with a substantial increase in sensitivity while maintaining the necessary dynamic range.

Taking advantage of full-quadrature phase detection and common-noise rejection, we experimentally demonstrate an increase of dynamic range by more than an order of magnitude in a single shot. Incorporating data from several consecutive shots, the dynamic range further increases in exponential fashion, allowing us to reach three orders of magnitude gain using only three measurements. Last, we demonstrate tracking of a dynamical signal with tens of radians shot-to-shot variation by combining the dual-T measurement with a particle filter protocol, representing a major improvement compared to recent works (*22*).

This approach can considerably enhance performance of sensors and, in particular, inertial-sensing atom interferometers, under challenging conditions, by enabling nonambiguous operation without sacrificing either sensitivity or bandwidth. Such conditions are encountered in field operation of such sensors, for example, in mobile gravity surveys or when used for inertial navigation on a moving platform. By extending the sensor real-time dynamic range, the requirements on vibration isolation or corrections based on auxiliary measurements can be relaxed or, equivalently, existing sensors can be operated in more demanding environments at higher sensitivities. Therefore, it complements and potentially improves the technique of hybridization with a classical sensor.

Dual-T measurements can be realized by multiple means, based on known atom interferometry tools, e.g., dual-species interferometry (*23*) or momentum-state multiplexing (*24*), in addition to phase shear readout (*27*) used in this work. It is also compatible with important atom interferometry practices, such as k-reversal (*33*, *34*) and zero–dead-time operation (*35*). Further improvement of the scheme is possible by incorporating more than two interferometric sequences within the same experimental shot, enabling the gain demonstrated here for sequential operation within a single shot. The dual-T approach may also be applied in other atom interferometers, such as gyroscopes in the butterfly configuration (*36*, *37*) and multiaxis inertial sensors in launched (*38*, *39*) or continuous (*40*) configurations.

MATERIALS AND METHODS

Details of the experiment

We load a cloud of ^{87}Rb atoms in a magneto-optical trap (MOT) and launch it upward at 0.9 m/s with moving optical molasses,

which also cools the cloud to 5 μK. Atoms initially populate equally all m_F sublevels in the $F = 2$ hyperfine manifold. We select atoms in two distinct velocity classes and in the $m_F = 0$ state using two counterpropagating Raman π pulses, with 20-μs duration and a relative Doppler detuning of 80 kHz. Two interferometric sequences of $\pi/2 - \pi - \pi/2$ pulses, with durations of 12, 24, and 12 μs, respectively, address each of the velocity classes as shown in Fig. 1. The timing of the π pulses of the two interferometers is set to 22 and 22.5 ms after the apex of the trajectories. The precise ratio of T_2/T_1 contains empirically calibrated corrections on the order of 10^{-5} with respect to the naïve $\sqrt{\tau}$ value, attributed mainly to finite Raman pulse durations (*41*). Before the final π/2 pulses, the Raman mirror is tilted by 120 μrad. With the MOT beams tuned on resonance with the $F = 2 \rightarrow F = 3$ cycling transition, a fluorescence image of atoms in the $F = 2$ level is taken on a charge-coupled device camera oriented perpendicularly to the Raman mirror tilt axis. The experiment is repeated every 2 to 3 s.

Extraction of the measured phases ϕ_1, ϕ_2

We first integrate the image horizontally to find the vertical Gaussian envelopes of the fringe patterns, which are used to define the analysis region of interest for each interferometer (fig. S2). We then vertically integrate the image over those regions and fit the resulting profile to Gaussian envelopes with sinusoidal modulation. The phases of the measurement are taken as the phases of the fitted fringes at the horizontal center of the cloud. Last, we calculate and correct the vibration-induced phase based on the auxiliary accelerometer signal (Nanometrics Titan), taking into account the different interrogation times of each interferometer.

Single-shot dual-*T* analysis

For each dual-*T* shot, we rotate the measured ϕ_1, ϕ_2 according to Eq. 3

$$\phi_{\mathrm{diff}} = \frac{2\pi}{1+\tau^2}\left(\frac{n_1}{D} - \Delta n\right) \tag{5}$$

$$\phi_{\mathrm{sum}} = \phi_a - 2\pi\frac{(n_1 + \tau n_2)}{1+\tau^2} \tag{6}$$

Within the extended dynamic range of $\pm D\pi$ for ϕ_a, the integer n_1 takes values within $\pm\lfloor D/2 \rfloor$, and $\Delta n = n_1 - n_2$ takes either 0 or ± 1. From ϕ_{diff}, we uniquely determine Δn

$$\Delta n = \begin{cases} 0 & |\phi_{\mathrm{diff}}| < \dfrac{\pi}{1+\tau^2}\left(1 - \dfrac{1}{2D}\right) \\ -\mathrm{sgn}(\phi_{\mathrm{diff}}) & |\phi_{\mathrm{diff}}| > \dfrac{\pi}{1+\tau^2}\left(1 - \dfrac{1}{2D}\right) \end{cases} \tag{7}$$

and n_1 follows as the round value of $D[(1+\tau^2)\phi_{\mathrm{diff}}/(2\pi) + \Delta n]$. Last, we estimate ϕ_a by substituting n_1 and $n_2 = n_1 - \Delta n$ back into ϕ_{sum}.

All measurements presented in this work were performed in a noisy urban-industrial environment and include passive vibration isolation and postprocessing correction of residual vibrations using the auxiliary accelerometer. The residual vibration phase noise is usually reduced to at most 200 mrad and post-processing correction of residual vibrations using the auxiliary accelerometer. By calculating the vibration-induced phase for each of the two interferometers based on their individual transfer function (*42*), the residual vibration phase noise is reduced to at most 300 mrad and typically below 200 mrad. However, as demonstrated in fig. S3, the dual-*T* approach works equally well also for substantially larger vibration noise (e.g., without correction based on the auxiliary accelerometer).

We focused the discussion on integer *D*. Rational *D* yields joint phase periodicity according to the lowest term numerator of *D* but with less efficient common-mode noise rejection. For irrational *D*, there is no well-defined periodicity and hence no discrete set of allowed ϕ_{diff} solutions. While, in both cases, dynamic range enhancement is attained, optimal results are achieved for integer *D*.

Sequential dual-*T* analysis

From a sequence of *N* ($N = 2,3$ in this work) shots with alternating $D^{(i)}$, where $i = 1, \ldots, N$, we retrieve *N* pairs of phases $[\phi_1^{(i)}, \phi_2^{(i)}]$. Analyzing each shot separately as described above, we extract from them a set of values $\tilde{n}_1^{(i)}$, each within $\pm\lfloor D^{(i)}/2 \rfloor$. Joint analysis of the sequential measurements in principle amounts to finding the integer n_1 that satisfies the set of equations $\tilde{n}_1^{(i)} = n_1 \bmod D^{(i)}$. The solution is unique within the range $\pm\mathrm{LCM}(D^{(1)}, \ldots, D^{(N)})$, LCM denoting the least common multiple. This analysis assumes that $n_1^{(i)} = n_1^{(1)}$ for all *i*, as the first interferometer always measures ϕ_a with the same interrogation time *T*. However, for values of ϕ_a close to odd multiples of π, phase noise may cause variations of up to ±1 in $n_1^{(i)}$. We calculate the variations $\Delta n_1^{(i)} = n_1^{(1)} - n_1^{(i)}$ for $i > 1$ as the round value of $(\phi_1^{(1)} - \phi_1^{(i)})/(2\pi)$ and take them into account when solving the set of equations described above for n_1. This estimation of $\Delta n_1^{(i)}$ is valid as long as ϕ_a does not change by more than π between shots, setting the limit for allowed ϕ_a variations for sequential dual-*T* analysis. In Fig. 2B, only measurements with $\Delta n_1^{(2)} = 0$ are shown for clarity; the full range of results is shown in fig. S4.

Experimental noise parameterization

Extending on Eqs. 1 and 2, we write the phases ϕ_1, ϕ_2 as

$$\phi_1 = (\phi_a + \delta\phi_{\mathrm{corr}}) + \delta\phi_{\mathrm{ind},1} - 2\pi n_1 \tag{8}$$

$$\phi_2 = \tau(\phi_a + \delta\phi_{\mathrm{corr}}) + \delta\phi_{\mathrm{ind},2} - 2\pi n_2 \tag{9}$$

Here, $\delta\phi_{\mathrm{corr}} \sim \mathcal{N}(0, \sigma_{\mathrm{corr}}^2)$ is the noise term on the inertial signal common to both interferometers, whereas $\delta\phi_{\mathrm{ind},1}, \delta\phi_{\mathrm{ind},2} \sim \mathcal{N}(0, \sigma_{\mathrm{ind}}^2)$ are independent noise terms, e.g., due to detection noise of each interferometer. While this noise parameterization is not completely general, we empirically observe that it describes our data extremely well, as demonstrated in Fig. 1F, and allows for convenient interpretation of the results, as demonstrated in Fig. 3C. We emphasize that the used methodology and data processing work well for any noise covariance. We further note that, while we identify the dominant contributions to $\delta\phi_{\mathrm{corr}}$ and $\delta\phi_{\mathrm{ind}}$ as vibration noise and detection noise, respectively, this correspondence is not complete. For example, vibrations at higher frequencies, for which the transfer functions of the two interferometers differ, would contribute to the estimate of the independent noise.

With this parameterization and based on Eq. 3, ϕ_{diff} and ϕ_{sum} are characterized by random noise with SDs $\sigma_{\mathrm{ind}}/\sqrt{1+\tau^2}$ and $\sigma_{\phi,\mathrm{est}} = \sqrt{\sigma_{\mathrm{corr}}^2 + \sigma_{\mathrm{ind}}^2/(1+\tau^2)}$, respectively. An outlier measurement occurs when the random deviation of ϕ_{diff} from its theoretical value is larger than half the difference between its discrete solutions, which is $2\pi/[D(1+\tau^2)]$. The probability of such an event is given by

$$\epsilon = \mathrm{erfc}\left(\frac{\pi}{\sqrt{2}}\frac{1}{D\sqrt{1+\tau^2}}\frac{1}{\sigma_{\mathrm{ind}}}\right) \quad (10)$$

and approximated by Eq. 4 for $\tau \approx 1$. See the Supplementary Materials for experimental noise characterization.

Systematic phase shifts

Dual-T measurements have several systematic phase shifts that are common also to conventional atom interferometers, due to factors such as one-photon light shifts, two-photon light shifts (*43*), and offset of the Raman frequency from Doppler resonance (*44*). Typically, either these effects are estimated and accounted for theoretically or they are eliminated through wave vector reversal (k-reversal) (*33*, *34*).

Nevertheless, some of these shifts may be complicated or modified by the existence of two simultaneous interferometer pulse sequences, while new sources of systematic shifts may arise, such as due to an estimation error of the cloud center position when using phase shear readout. As demonstrated in Fig. 4, these effects do not contribute to bias instability in the measured phase up to few milliradians, although they may introduce a constant bias, which can be determined and calibrated in advance by comparison of dual-T measurements with standard interferometry. We correct this bias by performing 15 to 50 initial calibration measurements for different D values and k_{eff} signs, where we assume prior knowledge of ϕ_a. For the time-varying experiment in Fig. 5, these calibration measurements are not included in the particle filter analysis.

Correction of drifts in the differential phase

As shown in fig. S5A, ϕ_{diff} exhibits small drifts over time from its expected discrete value. While these drifts do not directly enter into the estimation of ϕ_a, they may have a large impact on outlier probability ϵ. By performing k-reversal, we observe that the drift in ϕ_{diff} is antisymmetric with respect to k_{eff}. We therefore attribute the observed phase drifts to differential light shift between the two interferometric states of the Raman pulses. As the temporal response function to external phase shifts is antisymmetric with respect to the central π pulse, normally, the effect of light shifts due to the interferometer pulses cancels up to changes in the light shift during the interferometer due to laser intensity fluctuations (*45*). In our dual-T realization, the light shift induced by the $\pi/2$ pulses of the shorter interferometer on the longer one still cancels as before, but each interferometer experiences an uncompensated light shift owing to the π pulse of its counterpart. A realization of dual-T with simultaneous π pulses for both interferometers will circumvent this effect (*23*).

These mutual light shifts will be of approximately equal amplitude but opposite signs; therefore, they are suppressed in ϕ_{sum} by a factor $(1-\tau)/(1+\tau^2)$ but amplified in ϕ_{diff} by a factor $(1+\tau)/(1+\tau^2)$. These effects of light shifts are entirely canceled by performing k-reversal, and, as we observe in fig. S5B, the average value of ϕ_{diff} over $\pm k_{\mathrm{eff}}$ remains stable at time scales of 10^4 s to better than 1 mrad. In the particle filter demonstration, we used both k_{eff} signs to correct such drifts, demonstrating the compatibility of the k-reversal technique with the dual-T approach.

In addition, because of the discrete nature of ϕ_{diff}, the observed drifts can also be deterministically corrected without requiring k-reversal and thus with practically no impact on the interferometer performance or bandwidth. For the data presented in Figs. 2 and 3, we continuously correct drifts in ϕ_{diff}, without assuming prior knowledge of ϕ_a, by tracking the difference between the measured ϕ_{diff} values from the nearest discrete values and subtracting their long-term, moving average.

Particle filter implementation

We choose as state variables the instantaneous value of the inertial phase ϕ_a and its first- and second-order time derivatives, denoting

$$\boldsymbol{x}^{(m,i)} = [\phi_a^{(m,i)}\ \dot{\phi}_a^{(m,i)}\ \ddot{\phi}_a^{(m,i)}]^T \quad (11)$$

for the mth particle at the ith time step. As observables, we choose the two interferometer phases $\phi_{1,2}$. The initial value and derivatives of the input ϕ_a signal are approximately -207π, $8.6\pi/dt$, and $4.5\pi/dt^2$, respectively. We represent a scenario where some imperfect knowledge about the starting conditions exists by drawing the initial values of the particles from normal distributions characterized by

$$\begin{cases} \mu_\phi^{(0)} = -250\pi & \sigma_\phi^{(0)} = 50\pi \\ \mu_{\dot\phi}^{(0)} = 0 & \sigma_{\dot\phi}^{(0)} = 10\pi/dt \\ \mu_{\ddot\phi}^{(0)} = 0 & \sigma_{\ddot\phi}^{(0)} = 8\pi/dt^2 \end{cases} \quad (12)$$

At each time step of the filter, we first propagate the particles' state according to $\boldsymbol{x}^{(m,i+1)} = \mathbf{F}\cdot\boldsymbol{x}^{(m,i)} + \boldsymbol{w}^{(m,i)}$, with $\mathbf{F}$ being the state propagation matrix and $\boldsymbol{w}^{(m,i)}$ being a random process noise with zero mean and covariance matrix $\mathbf{Q}$. For our model, we have

$$\mathbf{F} = \begin{bmatrix} 1 & \mathrm{dt} & \frac{1}{2}dt^2 \\ 0 & 1 & \mathrm{dt} \\ 0 & 0 & 1 \end{bmatrix}, \mathbf{Q} = dt^2\begin{bmatrix} 0 & 0 & 0 \\ 0 & 0 & 0 \\ 0 & 0 & q_{\ddot a}^2 \end{bmatrix} \quad (13)$$

where dt is the time interval between consecutive measurements. Following state propagation, we calculate the expected interferometer signals for each particle as $\phi_1^{(m,i)} = \phi_a^{(m,i)}$ and $\phi_2^{(m,i)} = \tau^{(i)}\phi_a^{(m,i)}$, where $\tau^{(i)}$ is the scale factor ratio in the ith measurement. We calculate their residuals from the actual measurements modulo 2π and weigh each particle according to the likelihood that these residuals are consistent with the independent measurement noise σ_{ind}, which we take as 73 mrad according to the spread of $\delta\phi_{\mathrm{ind,diff}}$. State variable estimation is achieved by using a ridge-detection algorithm (MATLAB tfridge function) on the time-dependent particle histogram to estimate $\phi_{\mathrm{est}}^{(i)}$, as demonstrated in fig. S6. For $q_{\ddot a}$, we took a value of $6\pi/dt^2$, as it minimizes the mean error of the estimated ϕ_a from the measured $\phi_{1,2}$.

SUPPLEMENTARY MATERIALS

Supplementary material for this article is available at http://advances.sciencemag.org/cgi/content/full/6/45/eabd0650/DC1

REFERENCES AND NOTES

1. G. M. Tino, M. A. Kasevich, Atom interferometry, in *Proceedings of the International School of Physics "Enrico Fermi," Course CLXXXVIII* (Societa Italiana di Fisica and IOS Press, 2014).
2. T. Kovachy, P. Asenbaum, C. Overstreet, C. A. Donnelly, S. M. Dickerson, A. Sugarbaker, J. M. Hogan, M. A. Kasevich, Quantum superposition at the half-metre scale. *Nature* **528**, 530–533 (2015).

3. B. Barrett, L. Antoni-Micollier, L. Chichet, B. Battelier, T. Lévèque, A. Landragin, P. Bouyer, Dual matter-wave inertial sensors in weightlessness. *Nat. Commun.* **7**, 13786 (2016).
4. P. Haslinger, M. Jaffe, V. Xu, O. Schwartz, M. Sonnleitner, M. Ritsch-Marte, H. Ritsch, H. Müller, Attractive force on atoms due to blackbody radiation. *Nat. Phys.* **14**, 257–260 (2017).
5. D. Becker, M. D. Lachmann, S. T. Seidel, H. Ahlers, A. N. Dinkelaker, J. Grosse, O. Hellmig, H. Müntinga, V. Schkolnik, T. Wendrich, A. Wenzlawski, B. Weps, R. Corgier, T. Franz, N. Gaaloul, W. Herr, D. Lüdtke, M. Popp, S. Amri, H. Duncker, M. Erbe, A. Kohfeldt, A. Kubelka-Lange, C. Braxmaier, E. Charron, W. Ertmer, M. Krutzik, C. Lämmerzahl, A. Peters, W. P. Schleich, K. Sengstock, R. Walser, A. Wicht, P. Windpassinger, E. M. Rasel, Space-borne Bose-Einstein condensation for precision interferometry. *Nature* **562**, 391–395 (2018).
6. V. Xu, M. Jaffe, C. D. Panda, S. L. Kristensen, L. W. Clark, H. Müller, Probing gravity by holding atoms for 20 seconds. *Science* **366**, 745–749 (2019).
7. G. Rosi, F. Sorrentino, L. Cacciapuoti, M. Prevedelli, G. M. Tino, Precision measurement of the newtonian gravitational constant using cold atoms. *Nature* **510**, 518–521 (2014).
8. R. H. Parker, C. Yu, W. Zhong, B. Estey, H. Müller, Measurement of the fine-structure constant as a test of the standard model. *Science* **360**, 191–195 (2018).
9. R. Geiger, A. Landragin, S. Merlet, F. P. D. Santos, High-accuracy inertial measurements with cold-atom sensors. *AVS Quantum Sci.* **2**, 024702 (2020).
10. K. Bongs, M. Holynski, J. Vovrosh, P. Bouyer, G. Condon, E. Rasel, C. Schubert, W. P. Schleich, A. Roura, Taking atom interferometric quantum sensors from the laboratory to real-world applications. *Nat. Rev. Phys.* **1**, 731–739 (2019).
11. T. Farah, C. Guerlin, A. Landragin, P. Bouyer, S. Gaffet, F. Pereira Dos Santos, S. Merlet, Underground operation at best sensitivity of the mobile LNE-SYRTE cold atom gravimeter. *Gyroscopy Navig.* **5**, 266–274 (2014).
12. C. Freier, M. Hauth, V. Schkolnik, B. Leykauf, M. Schilling, H. Wziontek, H.-G. Scherneck, J. Müller, A. Peters, Mobile quantum gravity sensor with unprecedented stability. *J. Phys. Conf. Ser.* **723**, 012050 (2016).
13. V. Ménoret, P. Vermeulen, N. L. Moigne, S. Bonvalot, P. Bouyer, A. Landragin, B. Desruelle, Gravity measurements below 10^{-9} *g* with a transportable absolute quantum gravimeter. *Sci. Rep.* **8**, 12300 (2018).
14. Y. Bidel, N. Zahzam, C. Blanchard, A. Bonnin, M. Cadoret, A. Bresson, D. Rouxel, M. F. Lequentrec-Lalancette, Absolute marine gravimetry with matter-wave interferometry. *Nat. Commun.* **9**, 627 (2018).
15. X. Wu, Z. Pagel, B. S. Malek, T. H. Nguyen, F. Zi, D. S. Scheirer, H. Müller, Gravity surveys using a mobile atom interferometer. *Sci. Adv.* **5**, eaax0800 (2019).
16. Y. Bidel, N. Zahzam, A. Bresson, C. Blanchard, M. Cadoret, A. V. Olesen, R. Forsberg, Absolute airborne gravimetry with a cold atom sensor. *J. Geod.* **94**, 20 (2020).
17. S. Merlet, J. L. Gouët, Q. Bodart, A. Clairon, A. Landragin, F. Pereira Dos Santos, P. Rouchon, Operating an atom interferometer beyond its linear range. *Metrologia* **46**, 87–94 (2009).
18. J. Lautier, L. Volodimer, T. Hardin, S. Merlet, M. Lours, F. Pereira Dos Santos, A. Landragin, Hybridizing matter-wave and classical accelerometers. *Appl. Phys. Lett.* **105**, 144102 (2014).
19. R. Geiger, V. Ménoret, G. Stern, N. Zahzam, P. Cheinet, B. Battelier, A. Villing, F. Moron, M. Lours, Y. Bidel, A. Bresson, A. Landragin, P. Bouyer, Detecting inertial effects with airborne matter-wave interferometry. *Nat. Commun.* **2**, 474 (2011).
20. R. Dändliker, Y. Salvadé, *Springer Series in Optical Sciences* (Springer Berlin Heidelberg, 1999), pp. 294–317.
21. K. Falaggis, D. P. Towers, C. E. Towers, Multiwavelength interferometry: Extended range metrology. *Opt. Lett.* **34**, 950 (2009).
22. C. Avinadav, D. Yankelev, O. Firstenberg, N. Davidson, Composite-fringe atom interferometry for high-dynamic-range sensing. *Phys. Rev. Applied* **13**, 054053 (2020).
23. A. Bonnin, C. Diboune, N. Zahzam, Y. Bidel, M. Cadoret, A. Bresson, New concepts of inertial measurements with multi-species atom interferometry. *Appl. Phys. B* **124**, 181 (2018).
24. D. Yankelev, C. Avinadav, N. Davidson, O. Firstenberg, Multiport atom interferometry for inertial sensing. *Phys. Rev. A* **100**, 023617 (2019).
25. M. Kasevich, S. Chu, Atomic interferometry using stimulated raman transitions. *Phys. Rev. Lett.* **67**, 181–184 (1991).
26. M. Kasevich, D. S. Weiss, E. Riis, K. Moler, S. Kasapi, S. Chu, Atomic velocity selection using stimulated raman transitions. *Phys. Rev. Lett.* **66**, 2297–2300 (1991).
27. A. Sugarbaker, S. M. Dickerson, J. M. Hogan, D. M. S. Johnson, M. A. Kasevich, Enhanced atom interferometer readout through the application of phase shear. *Phys. Rev. Lett.* **111**, 113002 (2013).
28. S. M. Dickerson, J. M. Hogan, A. Sugarbaker, D. M. S. Johnson, M. A. Kasevich, Multiaxis inertial sensing with long-time point source atom interferometry. *Phys. Rev. Lett.* **111**, 083001 (2013).
29. Y.-J. Chen, A. Hansen, G. W. Hoth, E. Ivanov, B. Pelle, J. Kitching, E. A. Donley, Single-source multiaxis cold-atom interferometer in a centimeter-scale cell. *Phys. Rev. Applied* **12**, 014019 (2019).
30. C. Avinadav, D. Yankelev, M. Shuker, O. Firstenberg, N. Davidson, Rotation sensing with improved stability using point-source atom interferometry. *Phys. Rev. A* **102**, 013326 (2020).
31. P. Del Moral, Non linear filtering: Interacting particle solution. *Markov Process. Relat. Fields* **2**, 555–580 (1996).
32. R. van der Merwe, A. Doucet, N. de Freitas, E. A. Wan, *Advances in Neural Information Processing Systems* (Neural Information Processing Systems Foundation, Inc., 2001), pp. 584–590.
33. J. M. McGuirk, G. T. Foster, J. B. Fixler, M. J. Snadden, M. A. Kasevich, Sensitive absolute-gravity gradiometry using atom interferometry. *Phys. Rev. A* **65**, 033608 (2002).
34. A. Louchet-Chauvet, T. Farah, Q. Bodart, A. Clairon, A. Landragin, S. Merlet, F. Pereira Dos Santos, The influence of transverse motion within an atomic gravimeter. *New J. Phys.* **13**, 065025 (2011).
35. I. Dutta, D. Savoie, B. Fang, B. Venon, C. L. G. Alzar, R. Geiger, A. Landragin, Continuous cold-atom inertial sensor with 1 nrad/sec Rotation stability. *Phys. Rev. Lett.* **116**, 183003 (2016).
36. J. K. Stockton, K. Takase, M. A. Kasevich, Absolute geodetic rotation measurement using atom interferometry. *Phys. Rev. Lett.* **107**, 133001 (2011).
37. D. Savoie, M. Altorio, B. Fang, L. A. Sidorenkov, R. Geiger, A. Landragin, Interleaved atom interferometry for high-sensitivity inertial measurements. *Sci. Adv.* **4**, eaau7948 (2018).
38. B. Canuel, F. Leduc, D. Holleville, A. Gauguet, J. Fils, A. Virdis, A. Clairon, N. Dimarcq, C. J. Bordé, A. Landragin, P. Bouyer, Six-axis inertial sensor using cold-atom interferometry. *Phys. Rev. Lett.* **97**, 010402 (2006).
39. A. V. Rakholia, H. J. McGuinness, G. W. Biedermann, Dual-axis high-data-rate atom interferometer via cold ensemble exchange. *Phys. Rev. Applied* **2**, 054012 (2014).
40. J. M. Kwolek, C. T. Fancher, M. Bashkansky, A. T. Black, Three-dimensional cooling of an atom-beam source for high-contrast atom interferometry. *Phys. Rev. Applied* **13**, 044057 (2020).
41. B. Fang, N. Mielec, D. Savoie, M. Altorio, A. Landragin, R. Geiger, Improving the phase response of an atom interferometer by means of temporal pulse shaping. *New J. Phys.* **20**, 023020 (2018).
42. A. Peters, K. Y. Chung, S. Chu, High-precision gravity measurements using atom interferometry. *Metrologia* **38**, 25–61 (2001).
43. A. Gauguet, T. E. Mehlstäubler, T. Lévèque, J. L. Gouät, W. Chaibi, B. Canuel, A. Clairon, F. Pereira Dos Santos, A. Landragin, Off-resonant raman transition impact in an atom interferometer. *Phys. Rev. A* **78**, 043615 (2008).
44. P. Gillot, B. Cheng, S. Merlet, F. Pereira Dos Santos, Limits to the symmetry of a Mach-Zehnder-type atom interferometer. *Phys. Rev. A* **93**, 013609 (2016).
45. P. Cheinet, B. Canuel, F. Pereira Dos Santos, A. Gauguet, F. Yver-Leduc, A. Landragin, Measurement of the sensitivity function in a time-domain atomic interferometer. *IEEE Trans. Instrum. Meas.* **57**, 1141–1148 (2008).

Acknowledgments

Funding: This work was supported by the Pazy Foundation, the Israel Science Foundation, and the Consortium for quantum sensing of Israel Innovation Authority. **Author contributions:** D.Y. and C.A. built the apparatus, performed the measurements, and analyzed the data. N.D. and O.F. supervised the research. All authors contributed to the writing of the manuscript. **Competing interests:** The authors declare that they have no competing interests. **Data and materials availability:** All data needed to evaluate the conclusions in the paper are present in the paper and/or the Supplementary Materials. Additional data related to this paper may be requested from the authors.

Submitted 31 May 2020
Accepted 16 September 2020
Published 4 November 2020
10.1126/sciadv.abd0650

Citation: D. Yankelev, C. Avinadav, N. Davidson, O. Firstenberg, Atom interferometry with thousand-fold increase in dynamic range. *Sci. Adv.* **6**, eabd0650 (2020).